Environmental Science and Pollution Research (2018) 25:4761–4775
https://doi.org/10.1007/s11356-017-0855-8

RESEARCH ARTICLE

The synthetic evaluation of CuO-MnO_x-modified pinecone biochar for simultaneous removal formaldehyde and elemental mercury from simulated flue gas

Yaoyao Yi[1,2] · Caiting Li[1,2] · Lingkui Zhao[1,2,3] · Xueyu Du[1,2] · Lei Gao[1,2] · Jiaqiang Chen[1,2] · Yunbo Zhai[1,2] · Guangming Zeng[1,2]

Received: 5 August 2017 / Accepted: 27 November 2017 / Published online: 2 December 2017

Abstract

A series of low-cost Cu-Mn-mixed oxides supported on biochar (CuMn/HBC) synthesized by an impregnation method were applied to study the simultaneous removal of formaldehyde (HCHO) and elemental mercury (Hg^0) at 100–300° C from simulated flue gas. The metal loading value, Cu/Mn molar ratio, flue gas components, reaction mechanism, and interrelationship between HCHO removal and Hg^0 removal were also investigated. Results suggested that 12%CuMn/HBC showed the highest removal efficiency of HCHO and Hg^0 at 175° C corresponding to 89%and 83%, respectively. The addition of NO and SO_2 exhibited inhibitive influence on HCHO removal. For the removal of Hg^0, NO showed slightly positive influence and SO_2 had an inhibitive effect. Meanwhile, O_2 had positive impact on the removal of HCHO and Hg^0. The samples were characterized by SEM, XRD, BET, XPS, ICP-AES, FTIR, and H_2-TPR. The sample characterization illustrated that CuMn/HBC possessed the high pore volume and specific surface area. The chemisorbed oxygen (O_β) and the lattice oxygen (O_α) which took part in the removal reaction largely existed in CuMn/HBC. What is more, MnO_2 and CuO (or Cu_2O) were highly dispersed on the CuMn/HBC surface. The strong synergistic effect between Cu-Mn mixed oxides was critical to the removal reaction of HCHO and Hg^0 via the redox equilibrium of $Mn^{4+} + Cu^{+} \leftrightarrow Mn^{3+} + Cu^{2+}$.

Keywords Catalytic oxidation · CuO-MnO_x · Pinecone biochar · Formaldehyde · Element mercury

Introduction

Coal-fired power plants discharge many kinds of hazardous substances, such as volatile organic compounds (VOCs) and mercury (Hg). VOCs and Hg approximately accounts for 37% of total anthropogenic emissions (Chaggera et al. 1999; Fernandez-Martinez PL-M et al. 2001) and 17% of anthropogenic sources in China, respectively (Liu et al. 2016). It is generally known that VOCs and mercury are both harmful to human health and environment. If human beings stay in a certain volatile organic compounds concentration beyond the standard range for a long time, eyes and nose will be stimulated to get relevant sick and people will even have cancer (Zheng-Hong Huang et al. 2002). Formaldehyde (HCHO) is one of the volatile organic compounds and it causes many serious health problems, for instance, difficulty in breathing, nasopharyngeal, or nasal cancer (Zhang et al. 2009). Mercury is a global pollutant with persistence, bioaccumulation, and extreme toxicity (Zhang et al. 2017; Zhao et al. 2016a). Therefore, relevant laws and regulations about formaldehyde and mercury have been issued to prevent and control environmental pollution (Wang et al. 2004).

Responsible editor: Bingcai Pan

Electronic supplementary material The online version of this article (https://doi.org/10.1007/s11356-017-0855-8) contains supplementary material, which is available to authorized users.

✉ Caiting Li
ctli@hnu.edu.cn; ctli3@yahoo.com

[1] College of Environmental Science and Engineering, Hunan University, Changsha 410082, People's Republic of China

[2] Key Laboratory of Environmental Biology and Pollution Control, Ministry of Education, Hunan University, Changsha 410082, People's Republic of China

[3] College of Environmental Science and Resources, Xiangtan University, Xiangtan 411105, People's Republic of China

By far, sorbent-catalyst which can effectively remove HCHO is proved to be one of the most effective methods of removing Hg^0 (Wang et al. 2016). Hence, a high effective sorbent-catalyst needs to be developed to controlling the emission of HCHO and Hg^0. Different sorbents loaded active component (sorbent-catalysts) have been used in removing HCHO and Hg^0, such as Ce-Mn co-modified activated carbon (Wu et al. 2017), metallic oxide supported on Al_2O_3 (Álvarez-Galván et al. 2004; O'Shea et al. 2005), SiO_2 doped with TiO_2 (Erik et al. 2003), and zeolite (Abrishamkar and Kahkeshi 2013). Among these, activated carbon becomes one of the most promising sorbents for removing contaminants on account of its high surface area and vast porous structure. Activated carbon-loaded metal oxides have been proposed as sorbent-catalysts for controlling HCHO emission in many other researches (Dai et al. 2016). Besides, activated carbon-modified metal oxides (Wang et al. 2015) have also been studied as potential catalysts on the Hg^0 removal. Therefore, metal oxides loaded on activated carbon were developed as a potential adsorption catalytic material with extraordinarily high performance and they were employed in removing simultaneously HCHO and Hg^0. However, the high cost of commercial activated carbon restricts its application (Lee et al. 2016; Yang et al. 2016). Therefore, it is vital to research and exploit economical and effective support to replace activated carbon for the co-removal of HCHO and Hg^0. Recently, environment-friendly biochar with low-cost and rich porous structures as well as large specific surface have been attracting wide attention, which accords with the goal of sustainable development in nowadays society. The literature reported that modified biochar has high capacity on eliminating HCHO and Hg^0 (Bhandari et al. 2014; Yang et al. 2016). Hence, raw biochar modified by the use of chemical agent and (or) metal oxides may be a potential sorbent-catalyst replacing activated carbon-modified metal oxides for simultaneous removal of HCHO and Hg^0.

MnO_x are suggested to be optimal transition-metal compounds in environment-friendly materials and catalytic field (Morales et al. 2006). For example, Qu et al. (Qu et al. 2013) found that SO_2 removal performance of activated carbon was sharply improved by Mn loading. Lahousse et al. (Lahousse et al. 1998) suggested γ-MnO_2 was more active than noble metal catalysts for the oxidation of VOCs. Moreover, many researches indicated manganese-based catalyst possessed high redox capacity and it has been studied extensively in many catalytic fields, including for the capture of mercury (Evan et al. 2000; Qu et al. 2013; Tang et al. 2016; You et al. 2017; Granite et al. 2014; Uffalussy 2015).Granite first proposed that lattice oxygen oxidizes mercury in a Mars-Maessen mechanism (Evan et al. 2000). Interestingly, it was reported that supported CuO catalysts has been regarded as promising catalysts for the removal of VOCs and Hg^0 (Li et al. 2015; Tang et al. 2015). Besides, the combination of copper oxides with manganese oxides often results in the high catalytic performance. For example, Aguilera et al. (Daniel Antonio Aguilera et al. 2011) demonstrated the addition of copper content in mix Cu-Mn oxides could promote the generation of oxygen vacancies by preventing the manganese oxide from taking on a crystalline structure. Some researchers also suggested mixed Cu-Mn-based catalyst has great removal performance for pollutants, such as NO, VOCs, Hg^0, and SO_2 (Daniel Antonio Aguilera et al. 2011; Xingfu et al. 2008). In addition, copper and manganese oxides are used extensively because of their low cost. Therefore, it was deduced that Cu-Mn-mixed oxides supported on biochar might show excellent performance for HCHO and Hg^0 removal. However, the related research on the biochar-supported Cu-Mn-mixed oxides for simultaneous removal of HCHO and Hg^0 has rarely been reported. Meanwhile, the interrelationship between HCHO and Hg^0 as well as the removal mechanism of HCHO and Hg^0 are still not very clear.

Accordingly, in the present study, a series of Cu-Mn-mixed oxides supported on biochar (CuMn/HBC) were prepared to remove simultaneously HCHO and Hg^0 at 100–300 °C from simulated flue gas. The effects of the reaction temperature, metal loading value, Cu/Mn molar ratio, and flue gas components were investigated to explore the simultaneous removal performance of the samples for HCHO and Hg^0. The samples were characterized by SEM, XRD, BET, XPS, ICP-AES, FTIR, and H_2-TPR. These characterization results analyze the interrelationship between HCHO and Hg^0 as well as the reaction mechanism on the co-removal of HCHO and Hg^0.

Experimental section

Preparation of sample

Firstly, the pinecones were collected and washed using deionized water, dried, and grated. Secondly, the grated pinecones were sieved to get 80–100 mesh powder. Then the pinecone biochar was produced from being carbonized in tube furnace at 500 °C for 90 min with heating 5 °C/min under N_2 flow. The obtained products were denoted as biochar (BC). 30% H_2O_2 (1 g of BC per 10 ml of solution) impregnated the pinecone biochar for 24 h to obtain hydrogen peroxide activated biochar (HBC). Afterward, these samples were washed with distilled water to neutral and dried for 18 h at 105 °C.

A series of CuMn/HBC were prepared by impregnating HBC with a mixture solution containing appropriate quantity of $Mn(NO_3)_2$ and/or $Cu(NO_3)_2{\cdot}3H_2O$ for 24 h, then dried for 8 h at 105 °C. Afterward, it was put into a tube furnace to calcine at 500 °C for 4 h under N_2 atmosphere. The obtained samples were marked as ACu_xMn_y/HBC, in which x/y referred to the Cu/Mn molar ratio (x/y = 3:1, 2:1, 1:1, 1:2, 1:3,

1:4, 1:5) and *A* stood for the total metal oxides mass percentage on the samples (HBC + total metal oxides mass). Thereinto, CuMn/HBC also represented that the Cu/Mn molar ratio was 1:1. The single Mn/HBC and Cu/HBC were also prepared by the same method.

Catalytic performance test

The equipment chat of the simultaneous removal of formaldehyde and elemental mercury of catalysts is shown in Fig. 1. The peristaltic pump extracted 38% formaldehyde solution into a teflon tube which was packed with a temperature-controlled heating belt with heating to 110 °C, then solution was transformed into vapor. N_2 carried formaldehyde vapor in conical flask (placed in 80 °C thermostat water bath) into condensing unit for eliminating water vapor. 70 μg/m^3 Hg^0 was produced by a Hg^0 permeation tube (VICI Metronics, USA) which 100 mL/min pure N_2 passed through. Afterward, all gases entered into gas-mixed conical flask. Then the mixed gas passed through a fixed bed reactor which was a silica tube (i.d. 12 and 600 mm in length) placed vertically in a tubular electric furnace to stay the catalyst bed at desired temperature.

In each test, about 0.8-g sorbent-catalyst was placed in the fixed bed reactor. The total flow rate was commanded to 500 mL/min, and the corresponding gas hourly space velocity (GHSV) was approximately 13,000 h^{-1}. 6% O_2, 100 ppm HCHO, 70 μg/m^3 Hg^0, and balanced gas N_2 were composed of the simulated flue gas (SFG). And the influence part of flue gas components contained 400 or 800 ppm of SO_2 and 300 or 600 ppm of NO. The gas flow was exactly controlled by mass flow controller (MFC). Every experiment maintained 3 h in different conditions and temperature window extended 100 to 300 °C. The inlet and outlet concentrations of HCHO vapor and Hg^0 were, respectively, monitored by a PGM-7300(RAE, USA) and an online RA-915 M mercury analyzer (LUMEX Ltd., Russia). The Hg^0 removal efficiency (E_{Hg}) and HCHO conversion efficiency (E_{HCHO}) were, respectively, defined in Eqs. (1) and (2):

$$E_{Hg} = \left(1 - \frac{[Hg^0]_{out}}{[Hg^0]_{in}}\right) \times 100\% \quad (1)$$

$$E_{HCHO} = \left(1 - \frac{[HCHO]_{out}}{[HCHO]_{in}}\right) \times 100\% \quad (2)$$

where $[Hg^0]_{in}$ and $[HCHO]_{in}$, respectively, denote the inlet concentration of Hg^0 and HCHO. Similarly, $[Hg^0]_{out}$ and $[HCHO]_{out}$, respectively, stand for the outlet concentration. In order to recognize the speciation of mercury in the outlet gas, the mercury speciation conversion test was carried out. This part was discussed in Supplementary material.

Sample characterization

Scanning electron microscopy (SEM) aimed to observe the surface morphology and microstructure of the samples using

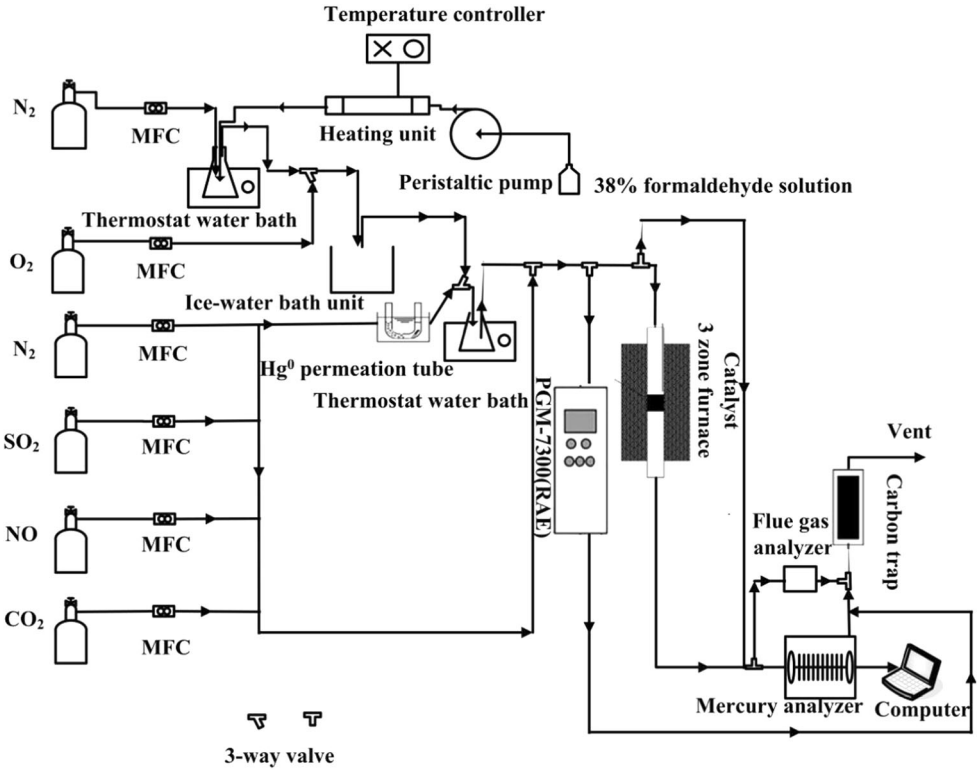

Fig. 1 Schematic diagram of the experimental setup

Quanta FEG 250. The image of each sample was magnified to ×5000 and 12%CuMn/HBC also was magnified to ×20,000. To obtain the Brunauer-Emmett-Teller (BET) specific surface area, average pore diameter, and pore volume of samples, a Micromeritics Tristar II 3020 analyzer (Micromeritics Instrument Crop, USA) was used. All samples kept at 150 °C for overnight and the operating temperature maintained 77 K. The actual metal content in samples was got by inductively coupled plasma-atomic emission spectroscopy (ICP-AES, SPECTRO BLUE SOP, Germany). The surface characteristics of the samples were analyzed by X-ray photoelectron spectroscopy (XPS). The K-Alpha 1063 X-ray photoelectron spectroscopy (Thermo Fisher Scientific, UK) emitted 72 W Al Kα radiation from micro aggregation monochromator. Powder X-ray diffraction (XRD) patterns were measured using a Rigaku D/Max 2500 with Cu Kα radiation and the 2θ range from 10° to 80°. The reducibility of samples were performed by the hydrogen temperature-programmed reduction (H_2-TPR) operated in a quartz tube equipped with a TCD detector (Peng xiang PX 200, China). An IR Prestige-21 spectrometer (Shimadzu, Japan) at the room temperature by the standard KBr disk method collected fourier transform infrared spectrometer (FTIR) spectra.

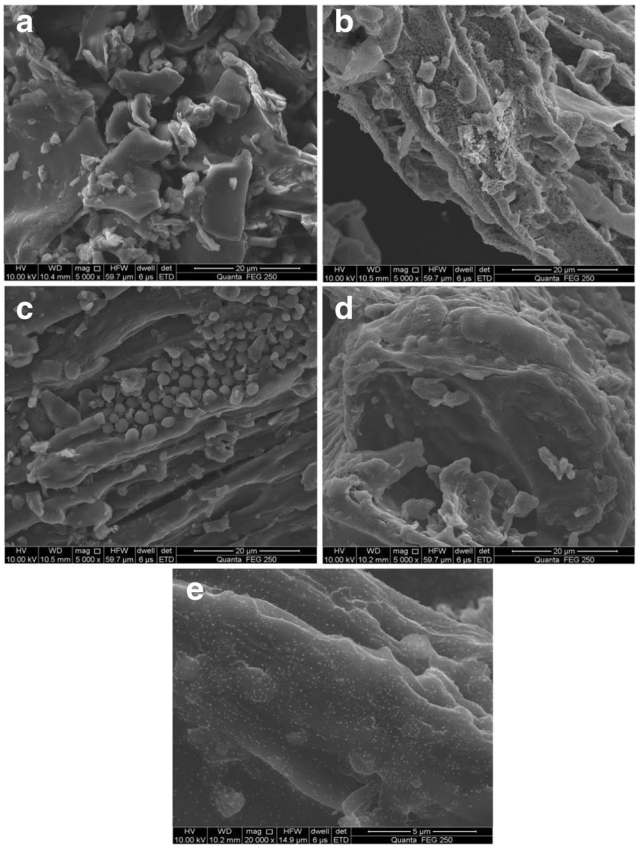

Fig. 2 SEM images of **a** HBC, **b** 12%Cu/HBC, **c** 12%Mn/HBC, **d** 12%CuMn/HBC(5000 X), and **e** 12%CuMn/HBC (20,000 X)

Results and discussion

Samples characteristics

SEM

Figure 2 represents the SEM images of the prepared samples. This figure revealed that the addition of metal oxide greatly influenced the microstructure of the HBC. For 12%Cu/HBC and some copper oxides were formed on the HBC surface. However, on the 12%Mn/HBC surface (Fig. 2c), no depositions were observed. Figure 2d, e show 12%CuMn/HBC microstructure images under ×5000 and ×20,000 magnification, respectively. 12%CuMn/HBC had no depositions on the surface under ×5000. Interestingly, Fig. 2e manifested the particles on the surface of 12%CuMn/HBC were observed which indicated metal oxides successfully supported on the HBC surface. During the preparation process, the interaction between metal precursors and HBC contributed to particles smaller and higher dispersion. The highly dispersed metal precursors on the surface of HBC could increase the catalytic activity to promote great removal performance for HCHO and Hg^0 (Xu et al. 2015).

BET

Table 1 shows the BET-specific surface area, average pore size, and pore volume of samples. The BET-specific surface area, average pore size, and pore volume of samples loaded with active CuO-MnO_x component were larger than those of the biochar. This might generate new pores in the process of impregnation and calcination (Sheng et al. 2017). Compared with 12%Mn/HBC, pore volume and specific surface area of 12%Cu/HBC diminished, which was in consistent with the results of SEM. Meanwhile, pore volume, BET-specific surface area, and average pore size of 12%CuMn/HBC was higher than that of 12%Mn/HBC and 12%Cu/HBC, which might be owed to the interaction of copper oxides and manganese oxides during the preparation process. At the same time, when the total metal oxides value gradually increased from 8 to 14%, pore volume and BET-specific surface area of samples increased firstly and then reduced. 12%CuMn/HBC had the highest pore volume and specific surface area, which was in agreement with the best removal performance. High surface area could supply more active sites and rich porous structure, which would be beneficial to adsorption and diffusion of reactant molecules (Tang et al. 2015). The 14% loading value made pore volume and specific surface area of the sample decrease due to the agglomeration of excessive metal oxides and blocking the internal micropore of HBC (Wu et al. 2015). When loading value was same ($12\%Cu_3Mn_1$/HBC, 12%CuMn/HBC, $12\%Cu_1Mn_3$/HBC), pore volume and

Table 1 BET-specific surface area, pore volume, and pore diameter of the samples

Sample	Specific surface area (m^2/g)	Pore volume (cm^3/g)	Average pore size (nm)
HBC	178.23	0.09	1.40
12%Cu/HBC	315.67	0.14	1.80
12%Mn/HBC	317.67	0.15	1.92
8%CuMn/HBC	318.20	0.15	1.94
12%Cu_3Mn_1/HBC	307.13	0.14	1.80
12%CuMn/HBC	320.98	0.16	2.02
12%Cu_1Mn_3/HBC	319.16	0.15	1.82
14%CuMn/HBC	308.94	0.15	1.88

surface area of samples reduced due to the increase of Cu or Mn content. Moreover, the enhancement of Cu content had a great effect on pore volume and surface area of samples in contrast with the augment of Mn content. The order of BET-specific surface area, pore volume of the samples roughly kept consistent with the removal efficiency. Therefore, the BET-specific surface area and pore volume of samples played important role in the activity of samples and removal performance.

XRD

In order to distinguish the crystal structures of samples, the X-ray diffraction profiles of prepared samples are displayed in Fig. 3. A diffraction peaks at 2θ = 26.482° was observed in all samples attributed to Graphite-C (PDF4 97-003-1829) (Wu et al. 2015). For 12%Mn/HBC, the diffraction peaks were detected at 2θ = 28.717°, 36.241°, and 34.840°, 40.421°, 58.62°, 70.037°, 73.76° corresponding to synthetic-Mn_3O_4 (PDF4 97-007-6088) (Wang et al. 2012) and Manganosite-MnO (PDF4 97–000-9864) (Guo et al. 2015), respectively.

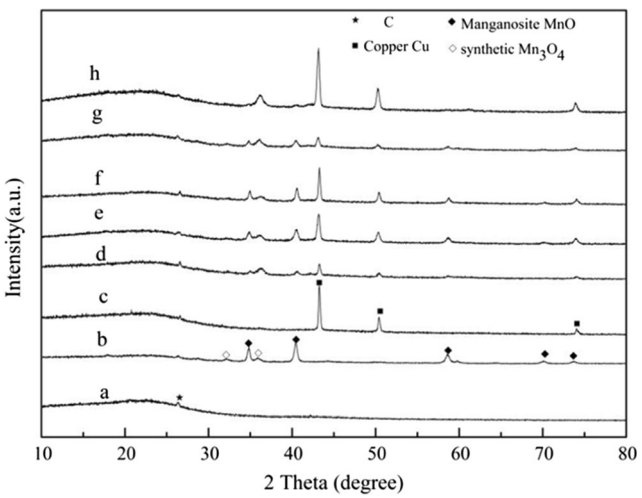

Fig. 3 XRD patterns of (a) HBC, (b) 12%Mn/HBC, (c) 12%Cu/HBC, (d) 8%CuMn/HBC, (e) 12%CuMn/HBC, (f) 14%CuMn/HBC, and (g) 12%Cu_1Mn_3/HBC, and; (h) 12%Cu_3Mn_1/HBC

The XRD pattern of 12%CuMn/HBC had no crystalline MnO_2 manifesting a highly dispersed or amorphous state on the HBC surface. Similarly, the main phase of 12%Cu/HBC was Copper—Cu (PDF4 01-070-3039) (Zhang et al. 2015) and no CuO or Cu_2O diffraction peaks were viewed. But, Cu^{2+}, and Cu^{+} were detected by XPS. Therefore, copper oxides were highly dispersed or existed as amorphous phase. The analytic results above also were in agreement with SEM. The amorphous or crystallite materials possessed enormous structure distortion to give more active sites for catalytic reactions comparing with crystalline materials (Liu et al. 2009; Zhang et al. 2017; Zhao et al. 2016a). Hence, HBC support promoted the dispersion of Cu-Mn mixed oxides on the surface and brought about high removal efficiency for HCHO and Hg^0 which accorded with the results of experiments and SEM. Increasing of the loading value, the high intensity of the diffraction peaks increased and 12%CuMn/HBC had a similar strength with 14%CuMn/HBC.

H2-TPR

H2-TPR investigated the reducibility of samples. As displayed in Fig. 4, the hydrogen consumption peaks of three sorbent-catalysts appeared around 610 to 640 °C attributed to the gasification of carbon support (Trépanier et al. 2009; Zhang et al. 2015). The H_2 reduction peaks of 12%Cu/HBC arose at 253 °C and that of 12%Mn/HBC appeared at 257 and 441 °C belong to the reduction of manganese oxide species. It was well documented that the hydrogen consumption peaks of pure CuO occurred at 260 °C (Morales et al. 2006; Shiau et al. 2006). Besides, some examples indicated that three reduction peaks of single-loaded Cu catalyst, respectively, attributed to the surface dispersed CuO, small CuO crystallites, and bulk CuO (Fei et al. 2014; Sheng et al. 2017). Therefore, the peak at 253 °C might be related to small CuO particles. For 12%Mn/HBC sample, it was reported that the temperature under 300 °C and above 300 °C attributed to MnO_x species to Mn_3O_4 and Mn_3O_4 to MnO, respectively (Tang et al. 2015). For 12%CuMn/HBC, the peak at 246 °C was ascribed to

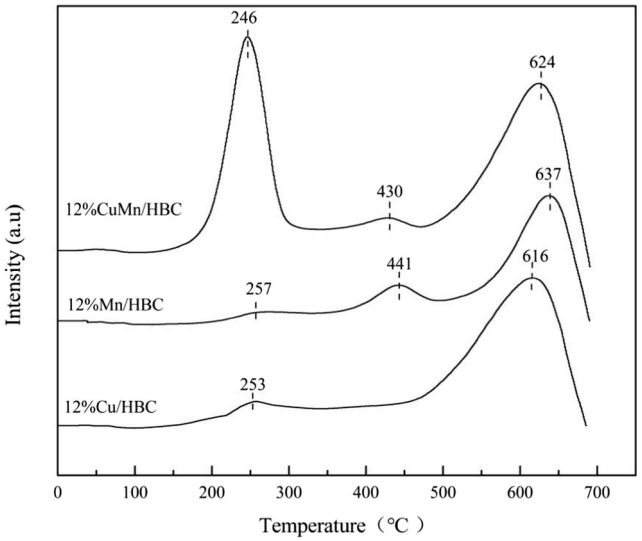

Fig. 4 H_2-TPR profiles of the samples

reduction of small CuO particles. The peak at 430 °C might be assigned to the reduction of Mn_3O_4 to MnO. The temperature of 12%CuMn/HBC reduction peaks shifted to lower than that of single samples declaring the presence of strong synergistic effect between copper and manganese oxides (Delimaris and Ioannides 2008; Tang et al. 2015). What's more, the H_2 reduction peaks area of 12%CuMn/HBC was larger than that of 12%Mn/HBC and12%Cu/HBC, which indicated the combination of Cu and Mn oxides greatly enhanced redox ability of sample. The sharp low-temperature reduction peak illustrated metal particles with uniform particle size distribution were highly dispersed (Xiaolan Tang et al. 2004). The difference of reduction peak of small CuO particles between 12%CuMn/HBC and 12%Cu/HBC contributed to the distinction of uniform CuO particle size distribution and dispersity. Obviously, the low-temperature reducibility of 12%CuMn/HBC was in good agreement with its excellent capacity for the removal HCHO and Hg^0. Contacted with results of BET and SEM, it was found that the combination of Cu and Mn influenced structural properties of samples, which contributed to promote the catalytic activity.

XPS

The transformation of chemical state and different elements content of fresh and spent samples were illustrated by XPS characterization analysis. The spectra of Cu2p, Mn2p, O1s, and Hg4f are depicted in Fig. 5. It was reported that the binding energy value of lattice oxygen (labeled as O_α) ranged from 529.3 to 530 eV, binding energy at 531.2–532 eV were defined as chemisorbed oxygen (labeled as O_β), and the BE of hydroxyl groups or/and adsorbed water species (labeled as O_γ) occurred near 534 eV (He et al. 2016; Huang et al. 2014; Li et al. 2011b). As exhibited in Fig. 5a, the O1s spectra of the fresh 12%Cu/HBC and 12%Mn/HBC were divided into three peaks at 530 eV (O_α), 531.9/531.4 eV (O_β), and 533.5/533.7 eV (O_γ), but only two peaks at 530 eV (O_α) and 531.8 eV (O_β) were observed in the fresh 12%CuMn/HBC. It can be deduced that the synergistic effect between Cu-Mn-mixed oxides increased the content of O_α and O_β as shown in Table 2. After simultaneous removal of HCHO and Hg^0 experiment was implemented, the content of O_α decreased from 31.82 to 18.21%, while O_β decreased from 68.18 to 55.95% and O_γ appeared as high as 25.84%. This situation manifested O_α and O_β took part in the reaction and the high content of O_α and O_β in 12%CuMn/HBC contributed to the great removal performance.

It is reported that the XPS signal of Mn2p3/2 were separated into three peaks at 641.4, 642.7, and 644.8 eV, respectively, corresponding to Mn^{3+}, Mn^{4+}, and the satellite (Tang et al. 2015; Xingyi et al. 2009; Ye et al. 2013). The Mn^{4+}/Mn^{3+} molar ratio are shown in Table 2. The more chemisorbed oxygen existed on the surface of 12%CuMn/HBC with the highest Mn^{4+}/Mn^{3+} molar ratio due to the form of Mn^{4+}-O_β Lewis acid-base pairs(Feng Quet al. 2013; Tang et al. 2015). The addition of Cu could enhance Mn^{4+} content which had strong synergistic effect between Cu and Mn. The Mn^{4+}/Mn^{3+} molar ratio of spent sample decreased from 2.43 to 0.84 which indicated that the reduction of Mn^{4+} to Mn^{3+} on the surface of sample conduced to HCHO conversion and Hg^0 oxidation in the reaction (He et al. 2014).

As displayed in Fig. 5c, the XPS spectra of Cu2p was divided into four peaks attributed to the Cu2p3/2 binding energy of 932.8 and 934.4 eV, the shake-up peak at 942–944 eV, and the Cu2p1/2 binding energy of 953–954 eV (Konsolakis et al. 2013; Peng et al. 2014). Some literatures suggested that BE at 934.2–934.5 eV, the Cu2p1/2 binding energy, and the shake-up peak can correspond to Cu^{2+} (Tang et al. 2015) and another Cu2p3/2 binding energy can be attributed to (Cu^++Cu^0) (Peng et al. 2014; Zhang et al. 2015). Hence, Cu^{2+} and (Cu^++Cu^0) specie existed on the surface of 12%Cu/HBC and 12%CuMn/HBC which was in agreement with the presence of Copper—Cu (PDF4 01-070-3039) in XRD results. However, the used 12%CuMn/HBC contained three peaks at 934.4, 943.2, and 954.7 eV assigned to Cu^{2+} specie. Therefore, Cu^+ specie shifted to Cu^{2+} specie in the reactions. From XPS analysis, the electron transfer between Cu and Mn was summarized by the equation: $Mn^{4+} + Cu^+ \leftrightarrow Mn^{3+} + Cu^{2+}$, which was critical to the removal reaction of HCHO and Hg^0.

Figure 5d shows the Hg4f spectrum of used 12%CuMn/HBC. The peaks appeared at 100.8 and 104.8 eV ascribed to HgO which indicated the oxidation of Hg^0 appeared on the surface of 12%CuMn/HBC, and the peak of Si2p (SiO_2) corresponded to 102.5 eV (He et al. 2014; Li et al. 2015). The XPS analysis illuminated that no characteristic peak of adsorbed Hg^0 was tested on the surface of sample. It could be

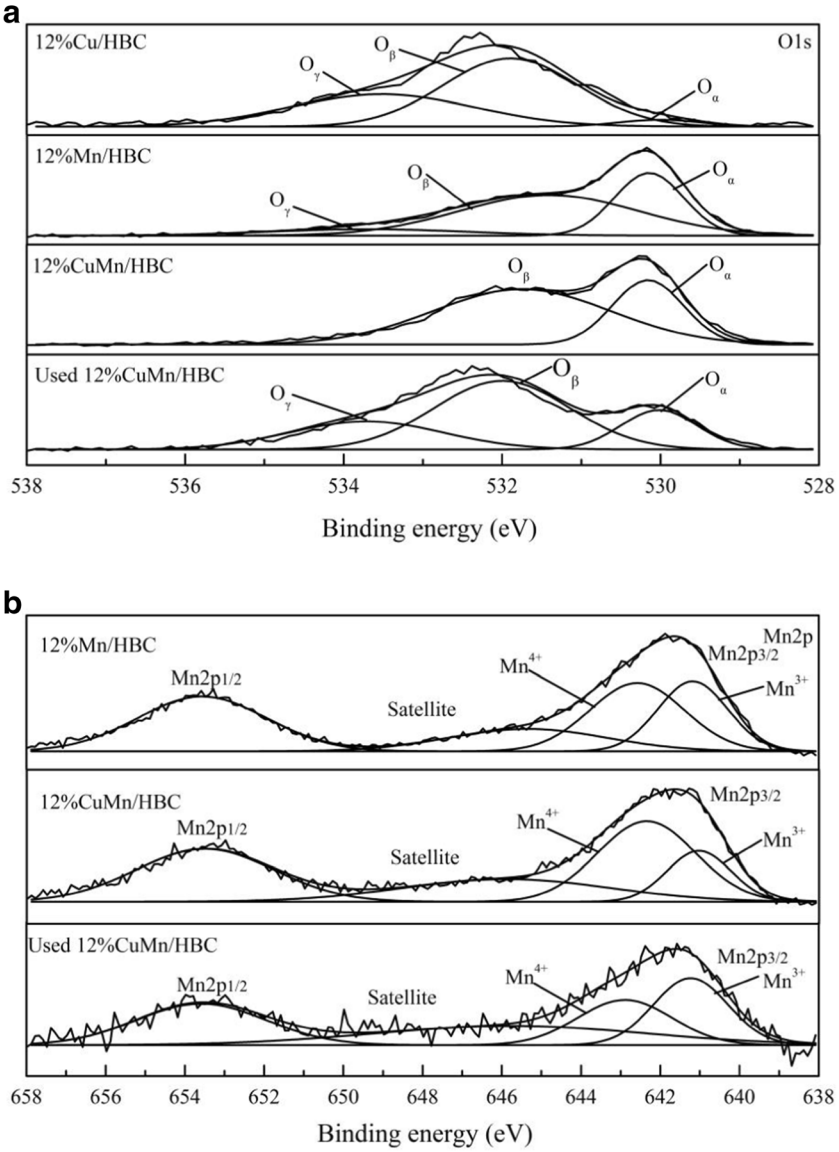

Fig. 5 XPS spectra of 12%Cu/HBC, 12%Mn/HBC, and fresh and used 12%CuMn/HBC over the regions of **a** O 1s, **b** Mn 2p, **c** Cu 2p, and **d** Hg 4f

speculated that Hg^0 was easily sublimed at 45 °C, adsorbed Hg^0 escaped from the surface of 12%CuMn/HBC at 175 °C; the content was below the limit of detection of XPS or when the sample was treated before XPS analysis, Hg^0 fled (He et al. 2014; Zhao et al. 2015). The Hg4f spectrum of used 12%CuMn/HBC indicated Hg^0 shifted mainly to HgO during the reactions.

FTIR

FTIR spectra of 12%CuMn/HBC adsorbing different gas components are shown in Fig. 6. The fresh 12%CuMn/HBC had nearly no characteristic peaks. But the band at 3750 cm^{-1} appeared the peaks of hydroxyl group bonding (Kwon et al. 2015). The band occurring near 1369 and 2950 cm^{-1} for used 12%CuMn/HBC were assigned as the symmetric stretch of (COO) and the CH stretch of bidentate formate (Ivanov et al. 2009; Ma et al. 2011). This indicated the form of intermediate products promoted ulteriorly the shift of HCHO to CO_2. The band at approximately 2370 cm^{-1} was ascribed to the CO_2 vibration. However, in the condition of HCHO + O_2 at 175 °C, the vibration of CO_2 did not appear due to the release of CO_2 at the high temperature. Some studies suggested the band at the range of 1479–1575 cm^{-1} were attributed to NO_2-containing compounds accelerating Hg^0 oxidation and 1575 cm^{-1} can be ascribed to nitrite or nitrate species (He et al. 2016; Jin et al. 2010). When SO_2 was added into the simulated flue gas, the band at around 1120 and 1230 cm^{-1} appeared. Hence, it can be ascribed to the bidentate sulfato-metal surface complexes or bidentate-surface (HSO_4^-、SO_4^{2-}) (Hongbo et al. 2007). Therefore, these analyses indicated NO, SO_2, and HCHO had competitive adsorption, but the form of NO_2-containing

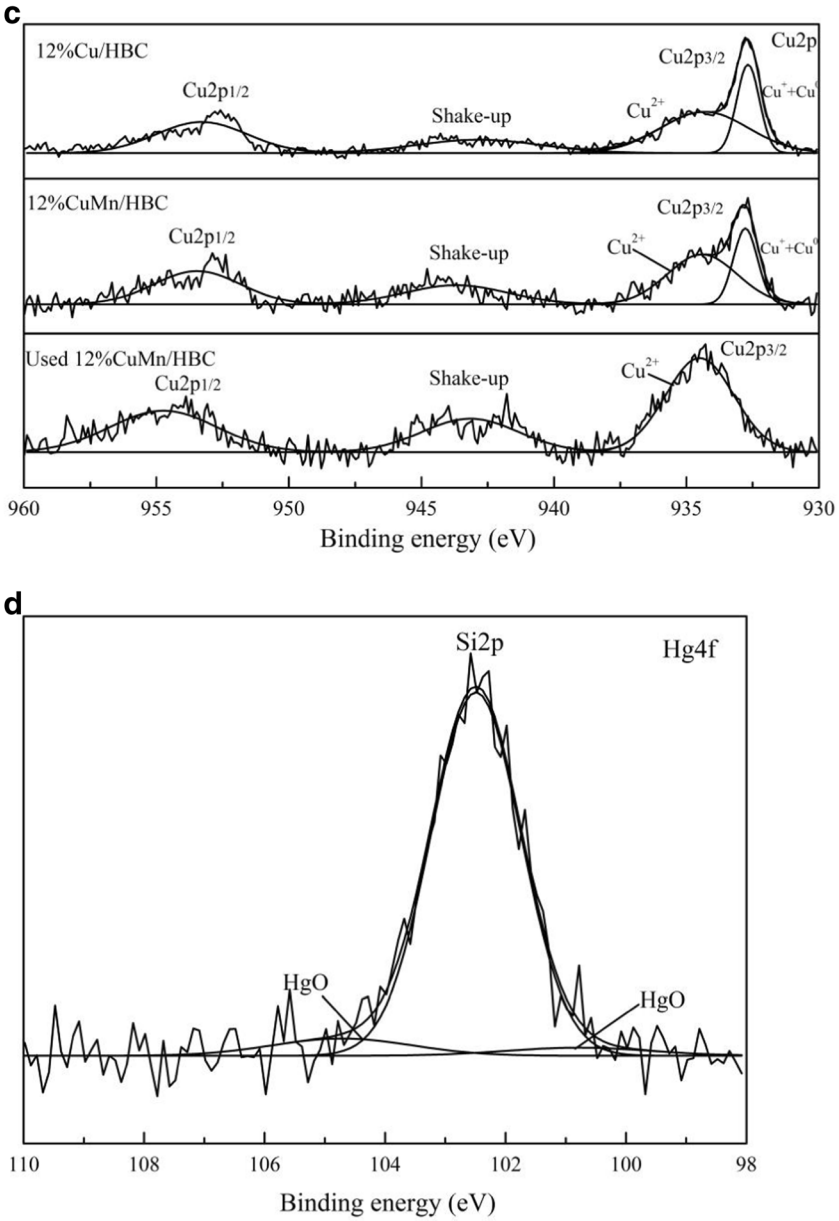

Fig. 5 (continued)

Table 2 Elemental contents of 12%Cu/HBC, 12%Mn/HBC, 12%CuMn/HBC, and used 12%CuMn/HBC from XPS analysis

Sample	Ratio of the oxygen			Cu^{+}/Cu^{2+}	Mn^{4+}/Mn^{3+}
	O_{α}	O_{β}	O_{γ}		
12%Cu/HBC	3.61	58.68	37.71	0.25	–
12%Mn/HBC	33.72	56.47	9.81	–	1.32
12%CuMn/HBC	31.82	68.18	–	0.22	2.43
used 12%CuMn/HBC	18.21	55.95	25.84	0	0.84

compounds promoted Hg^0 oxidation. The intermediate products were generated during the conversion process of HCHO.

The performance of different samples

Effect of reaction temperature and loading value

A series of samples with different loading value of Cu-Mn-mixed oxides were placed in a fixed bed reactor to study the simultaneous removal efficiency of HCHO and Hg^0. Formaldehyde conversion and Hg^0 removal efficiency of samples at the reaction temperature of 100–300 °C are shown in

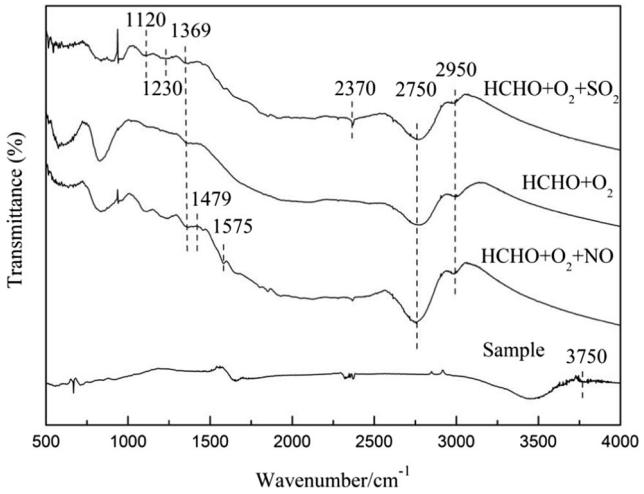

Fig. 6 FTIR spectra of fresh and used 12%CuMn/HBC. Reaction condition: $HCHO + O_2$: 6% O_2, 100 ppm HCHO, N_2 as balance gas, $T = 175$ °C; $HCHO + O_2 + NO$: 6% O_2, 100 ppm HCHO, 300 ppm NO, N_2 as balance gas, $T = 30$ °C; and $HCHO + O_2 + SO_2$: 6% O_2, 100 ppm HCHO, 400 ppm SO_2, N_2 as balance gas, $T = 30$ °C; 500 mL/min total flow rate, GHSV = 13,000 h^{-1}

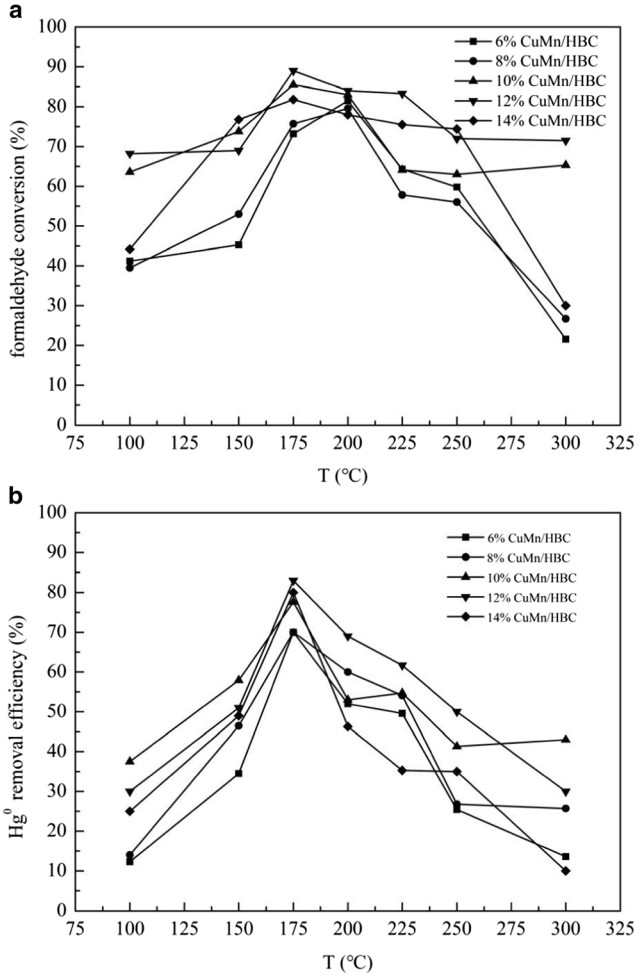

Fig. 7 Effect of loading value and reaction temperature on the removal of HCHO and Hg^0 over CuMn/HBC. **a** Formaldehyde conversion. **b** Hg^0 removal efficiency. Reaction condition: 6% O_2, 100 ppm HCHO, 70 μg/m^3 Hg^0, N_2 as balance gas, 500 mL/min total flow rate, and GHSV = 13,000 h^{-1}

Fig. 7. All samples at low or high temperatures (100 or 300 °C) presented poor removal capacity for HCHO and Hg^0. As displayed in Fig. 7, it was found the reaction temperature had an obvious impact on the performance for simultaneous removal of HCHO and Hg^0. The formaldehyde conversion and Hg^0 removal efficiency firstly increased as the reaction temperature increased from 100 to 175 °C and all samples presented high removal efficiency of HCHO and Hg^0 at 175 °C. However, when the reaction temperature further increased, catalytic activity decreased distinctly. In addition, it was clear that the total metal oxides mass percentage influenced the activity of sorbent-catalysts. It could be seen that HCHO conversion performance of samples with loading value from 6 to 14% did not exhibit specific trend. While the removal performance of Hg^0 firstly increased and then decreased with the increasing of loading value. 12%CuMn/HBC had best removal efficiency of HCHO and Hg^0 at 175 °C corresponding to 89 and 83%, respectively. The possible reason was that the excessive metal oxides deposited over the external surface of HBC, resulting in the decrease of pore volume, average pore size, and specific surface area of sample (as shown in Table 1). Besides, the ICP results also indicated excess loading value (14%) did not make the actual content grow obviously. The best removal performance of 12%CuMn/HBC may be contributed to the largest species surface area and the high content of O_α and O_β as well as highest Mn^{4+}/Mn^{3+} molar ratio from XPS analysis. Besides, H_2-TPR results suggested 12%CuMn/HBC had good redox properties.

The actual metal oxides value was obtained by the ICP-AES (Table 3). The actual CuO and MnO_2 content in different samples were a little higher than that in the academic loading content on account of the decrease of biochar mass during calcination process. The ICP results illustrated that actual and academic loading value had little difference.

Effect of Cu/Mn molar ratio

Simultaneous removal of HCHO and Hg^0 of 12%Cu_xMn_y/HBC with diverse Cu/Mn molar ratios are displayed in Fig. 8. The removal performance of HCHO and Hg^0 significantly decreased when the molar ratios of Cu and Mn were increased from 1:1 to 3:1 or reduced from 1:1 to 1:5. When molar ratio of Cu and Mn was 1:1, the sample had best removal activity of HCHO and Hg^0. As displayed in Table 1, 12%Cu_1Mn_1/HBC possessed the highest specific surface area and pore volume, and the specific surface area and pore volume of 12%Cu_3Mn_1/HBC and 12%Cu_1Mn_3/HBC decreased. It was inferred that the texture properties of samples were influenced due to the change of Cu/Mn molar ratio. Besides, when molar ratio of Cu and Mn was 1:1, the synergetic

Table 3 The actual metal content in different catalysts from ICP results

Catalysts	Metal oxide content (wt%)	
	CuO	MnO_2
6%CuMn/HBC	2.95	3.25
8%CuMn/HBC	3.70	4.20
10%CuMn/HBC	4.90	5.48
12%CuMn/HBC	6.09	7.10
14%CuMn/HBC	6.79	7.67

interaction between Cu and Mn reached the best balanced state. In contrast with 12%Cu/HBC and 12%Mn/HBC, 12%CuMn/HBC demonstrated great removal efficiency. The reason was that the synergetic interaction between Cu and Mn oxides improved the reducibility of sample. HBC possessed a better removal performance for formaldehyde and element mercury comparing with BC. When carriers were different (12%CuMn/BC and 12%CuMn/HBC), it was apparently found that 12%CuMn/HBC had high removal capacity for two pollutants.

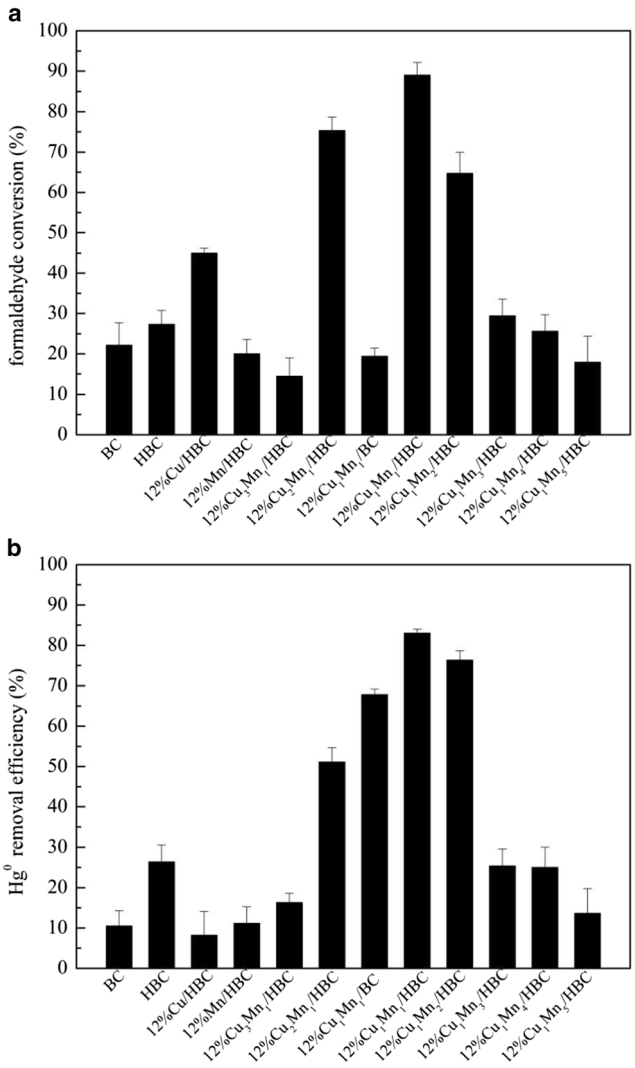

Fig. 8 Effect of different Cu/Mn molar ratios on the removal of HCHO and Hg^0 over samples. **a** Formaldehyde conversion. **b** Hg^0 removal efficiency.
Reaction condition: 6% O_2, 100 ppm HCHO, 70 μg/m^3 Hg^0, N_2 as balance gas, 500 mL/min total flow rate, and GHSV = 13,000 h^{-1}.

Stability test of the sample

The removal efficiency of the stability test of samples as well as the efficiency of HCHO conversion to CO_2 are displayed in Fig. 9. The stability test of 12%CuMn/HBC continued for 48 h. Firstly, it was noted that the efficiency of HCHO conversion to CO_2 was higher than 90%. For 15 h prior, the removal efficiency of HCHO and Hg^0 were instability and the later remained basically stability floating from 80 to 70%. Because of limited adsorption ability of sample and the consumption of active site and component, the removal efficiency of samples decreased during 48 h. After stability, the removal efficiency of HCHO and Hg^0 still kept at around 70% which could gas-phase O_2 regenerated and replenished O_α and O_β (Li et al. 2011a; Zhao et al. 2016a). This test indicated 12%CuMn/HBC had better stability to apply in the practical application.

Effect of gas components on the removal of HCHO and Hg^0

Figure 10 displays the impact of various gas components on the co-removal of HCHO and Hg^0. It was obvious that the removal performance of HCHO and Hg^0 increased with the increase of O_2 concentration from 0 to 12%. Compared with absence of O_2, the addition of 6% O_2 significantly improved the removal efficiency of HCHO and Hg^0. It may be deduced that the lattice oxygen and the chemisorbed oxygen which played a key role in the reaction were regenerated by gas-phase O_2 (Li et al. 2011a; Zhao et al. 2016a). When 6% O_2 further enhanced to 12%, the removal efficiency of 12%CuMn/HBC slightly increased. This phenomenon suggested 6% O_2 was sufficient for Hg^0 oxidation as well as HCHO conversion and excessive O_2 had little impact.

NO with 300 ppm or 600 ppm was added into total gas to study the effect of NO. NO suppressed the HCHO removal and promoted the Hg^0 removal. The inhibitive effect on the HCHO removal may be inferred that NO took up the active sites faster than HCHO due to its small molecular matter and consumed O_α and O_β to form the NO_2-containing compounds and nitrate observed in FTIR spectra (Sheng et al. 2017). These adsorbed species had competitive adsorption with Hg^0 and HCHO. However, the NO_2-containing compounds of the broad peaks at 1479–1575 cm^{-1} promoted Hg^0 oxidation (He et al. 2016).

The effect of SO_2 also was investigated in the condition of the addition of 400 or 800 ppm SO_2. It was observed that the

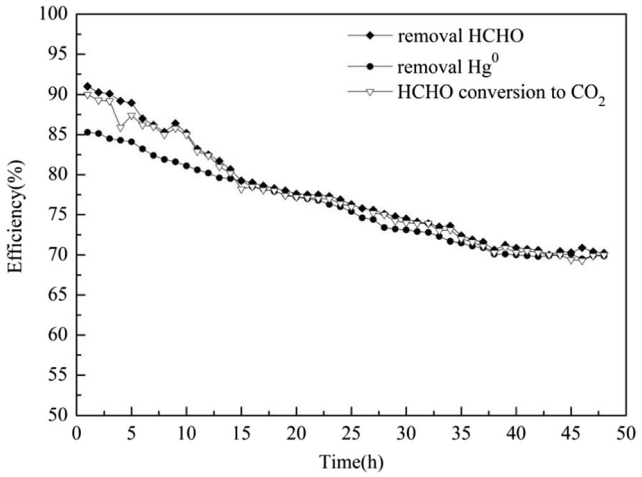

Fig. 9 Stability test of 12%CuMn/HBC for the removal of HCHO and Hg^0. Reaction condition: 6% O_2, 100 ppm HCHO, 70 μg/m^3 Hg^0, N_2 as balance gas, T = 175 °C, 500 mL/min total flow rate, and GHSV = 13,000 h^{-1}

HCHO removal efficiency decreased from 89 to 75.1% in the presence of 800 ppm SO_2 and the removal performance of Hg^0 declined from 83 to 68.3%. The inhibitive effect of SO_2 on the removal of two contaminants attributed to the competitive adsorption between SO_2 and two contaminants contacting with FTIR analysis and the generation of metal sulfates on the catalyst surface (He et al. 2016). The form of metal sulfates was irreversible which made the content of active component decrease, then resulted in the decrease of the content of lattice oxygen and surface active oxygen. Besides, because SO_4^{2-} belongs to strong-binding species, the reactions of Hg^0 oxidation and HCHO conversion were suppressed (Saha et al. 2013).

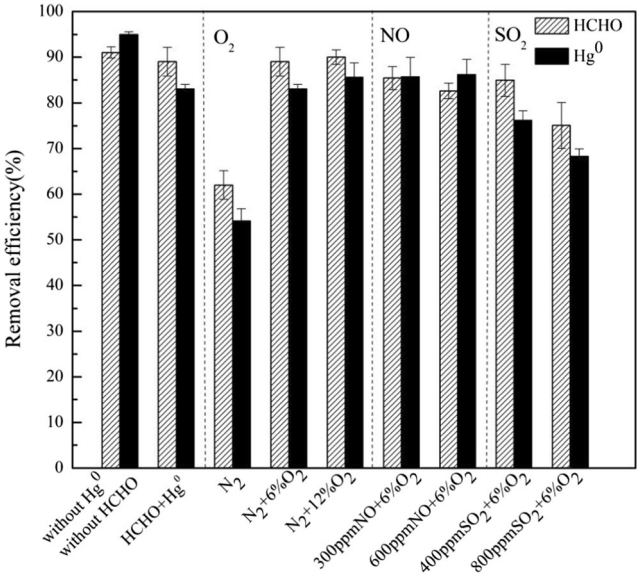

Fig. 10 Effect of individual flue gas components on the removal of HCHO and Hg^0 over 12%CuMn/HBC. Reaction condition: 6% O_2, 100 ppm HCHO, 70 μg/m^3 Hg^0, N_2 as balance gas, T = 175 °C, 500 mL/min total flow rate, and GHSV = 13,000 h^{-1}

Effect of HCHO and Hg^0

The interaction effect between HCHO and Hg^0 is displayed in Fig. 10. HCHO removal efficiency in the absence of Hg^0 was slightly higher than that in the presence of Hg^0. It indicated that the presence of Hg^0 had little suppressive impact on the removal of HCHO because Hg^0 concentration (70 μg/m^3) was little than the HCHO concentration (100 ppm). However, the addition of HCHO had a great influence on the removal performance of Hg^0 decreasing from 95 to 83%. That reason was that high HCHO concentration contributed to adsorption and oxidation in competition process with Hg^0. The following had detail experiment on the influence of the addition of HCHO.

As displayed in Fig. 11, the further experiment was implemented to investigate the influence of HCHO on the Hg^0 removal efficiency. It was found that after the addition of HCHO, the removal performance of Hg^0 sharply decreased because of the existence of competitive adsorption and oxidation between HCHO and Hg^0. After withdrawing HCHO, the removal efficiency of Hg^0 recovered. This result indicated the activity of sorbent-catalyst was not influenced. The reasons were that HCHO combined with active cite and reacted with surface active oxygen to generate gas-phase CO_2 which active cite could be exposed and the addition of 6%O_2 replenished surface active oxygen.

Mechanism discussion

FTIR results illustrated the intermediate products (the symmetric stretch of (COO) and the CH stretch of bidentate formate) generated during the conversion process of HCHO. XPS analysis indicated that the copper and manganese oxides existed on the surface of samples and had electron transfer. Combined with characterization analysis and experiment results, the mechanism of HCHO removal was speculated. Firstly, HCHO was adsorbed on the surface of samples. Then surface active oxygen which was produced from CuO-MnO_x attacked the C–H of HCHO to form the formate and the C–H of formate subsequently combined with the surface active oxygen to produce bicarbonate species (Ma et al. 2011). Then bicarbonate species attached H^+ to form carbonic acid which could decompose into CO_2 and H_2O. The HCHO removal mechanism was summarized as follows:

$$HCHO_{(g)} \rightarrow HCHO_{(ad)} \quad (3)$$

$$2CuO \rightarrow Cu_2O + O^* \quad (4)$$

$$2MnO_2 + Cu_2O \rightarrow Mn_2O_3 + 2CuO \quad (5)$$

$$2MnO_2 \rightarrow Mn_2O_3 + O^* \quad (6)$$

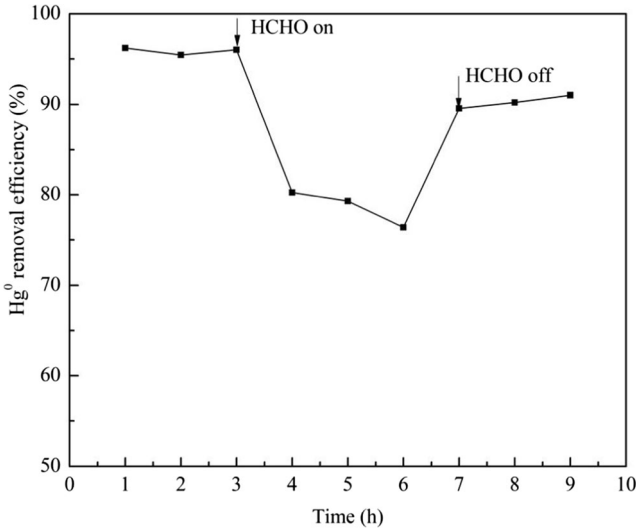

Fig. 11 Effect of HCHO on the removal of Hg^0 over 12%CuMn/HBC. Reaction condition: 6% O_2, 100 ppm HCHO, 70 μg/m^3 Hg^0, N_2 as balance gas, T = 175 °C, 500 mL/min total flow rate, and GHSV = 13,000 h^{-1}

$$HCHO_{(ad)} + 2MnO_2 \rightarrow \bullet CHO + H^+ + O^{*-} + Mn_2O_3 \quad (7)$$

$$\bullet CHO + O^{*-} \rightarrow HCOO^- \quad (8)$$

$$HCOO^- + H^+ \rightarrow HCOOH \quad (9)$$

$$HCOOH + 2MnO_2 \rightarrow HCOO\bullet + H^+ + Mn_2O_3 \quad (10)$$

$$HCOO\bullet + O^{*-} \rightarrow HCO_3^- \quad (11)$$

$$HCO_3^- + H^+ \rightarrow H_2CO_3 \quad (12)$$

$$H_2CO_3 \rightarrow CO_{2(g)} + H_2O_{(g)} \quad (13)$$

XPS results illustrated lattice oxygen and O_β participated in the reaction and the electron transfer between Cu and Mn was summarized by the equation: $Mn^{4+} + Cu^+ \leftrightarrow Mn^{3+} + Cu^{2+}$. The Hg4f spectrum in XPS analysis and the experimental data indicated Hg^0 was mainly oxidized into HgO. It was reported Hg^0 was oxidized by the lattice oxygen ([O]) which was produced by the metal transfer (Zhao et al. 2016b) or the chemisorbed oxygen (O_β) to generate HgO (He et al. 2014; Zhang et al. 2017). Therefore, according to the characterization results and other studies, the removal mechanism of Hg^0 over CuO-MnO_x/HBC was inferred as follows: firstly, gas-phase Hg^0 was adsorbed on the surface of samples. Subsequently, [O] and O_β took part in oxidation reaction which made adsorbed Hg^0 oxidize into HgO. Part of adsorbed HgO shifted to gas-phase HgO. The mechanism was described as follows:

$$O_2 \rightarrow O_\beta \quad (14)$$

$$Hg^0_{(g)} \rightarrow Hg^0_{(ad)} \quad (15)$$

$$2CuO \rightarrow Cu_2O + [O] \quad (16)$$

$$2MnO_2 + Cu_2O \rightarrow Mn_2O_3 + 2CuO \quad (5)$$

$$2MnO_2 \rightarrow Mn_2O_3 + [O] \quad (17)$$

$$Hg^0_{(ad)} + [O] \rightarrow HgO \quad (18)$$

$$Hg^0_{(ad)} + O_\beta \rightarrow HgO \quad (19)$$

$$HgO_{(ad)} \rightarrow HgO_{(g)} \quad (20)$$

Finally, the addition of 6% O_2 made low chemical state of metal oxides shift to high chemical state which could continue to replenish surface active oxygen and lattice oxygen. The equations were summarized as follows:

$$Mn_2O_3 + \frac{1}{2}O_2 \rightarrow 2MnO_2 \quad (21)$$

$$Cu_2O\left(Cu^0\right) + \frac{1}{2}O_2 \rightarrow CuO \quad (22)$$

Conclusions

A series of CuMn/HBC sorbent-catalysts were prepared by impregnating method and 12%CuMn/HBC showed greatest removal efficiency of HCHO and Hg^0 at 175 °C. Coal-derived flue gas is a complex mixture containing fly ash particles, oxygen, moisture, carbon monoxide, and many acid gases. A typical untreated flue gas derived from the combustion of a US Low Sulfur Eastern bituminous coal can contain: 5–7% H_2O, 3–4% O_2, 15–16% CO_2, 1 ppb total Hg, 20 ppm CO, 10 ppm hydrocarbons, 100 ppm HCl, 800 ppm SO_2, 10 ppm SO_3, 500 ppm NO_x, and balance N_2 (Granite and Pennline 2002; Presto and E.J 2007; Presto et al. 2007). In the effect of gas components of tests, O_2 had positive impact on the removal of HCHO and Hg^0. Besides, NO showed slightly positive influence and SO_2 had an inhibitive effect on the removal efficiency of Hg^0, while NO and SO_2 both exhibited prohibitive impact on the HCHO conversion efficiency. The testing system employed in our work did not include CO, SO_3, NO_2, and HCl species present in flue gas. There can be potential impacts of both carbon monoxide and acid gases such as SO_3, NO_2, and HCl upon the capture of mercury, and this could be a fruitful area for future study and research. In the part of the interrelationship between HCHO and Hg^0, the addition of HCHO had a great influence on the removal performance of Hg^0, but the presence of Hg^0 had little effect on the removal of HCHO. 12%CuMn/HBC had the highest specific surface area and pore volume from the characterization analysis. What is more, H_2-TPR analysis showed the presence of strong synergistic effect between Cu and Mn. MnO_2 and CuO in the CuMn/HBC were highly dispersed or amorphous state obtained from XRD and XPS analysis. XPS results illustrated O_α and O_β took part in the reaction and the high content of O_α and O_β in 12%CuMn/HBC contributed to the great removal

performance. Therefore, 12%CuMn/HBC is a promising sorbent-catalyst for the removal of formaldehyde and elemental mercury. On the side, the attrition resistance of the sorbent can be an important parameter for commercial applications and it will be examined in future research.

Funding information This work was financially supported by the National Natural Science Foundation of China (51478173), the National Key Research and Development Program of China (2016YFC0204100), and the Scientific and Technological Major Special Project of Hunan Province in China (2015SK1003).

References

Abrishamkar M, Kahkeshi FB (2013) Synthesis and characterization of nano-ZSM-5 zeolite and its application for electrocatalytic oxidation of formaldehyde over modified carbon paste electrode with ion exchanged synthesized zeolite in alkaline media. Microporous Mesoporous Mater 167:51–54. https://doi.org/10.1016/j.micromeso.2012.04.040

Álvarez-Galván MC, Pawelec B, de la Peña O'Shea VA, Fierro JLG, Arias PL (2004) Formaldehyde/methanol combustion on alumina-supported manganese-palladium oxide catalyst Appl Catal B Environ 51:83–91 doi:https://doi.org/10.1016/j.apcatb.2004.01.024, 2

Bhandari PN, Kumar A, Bellmer DD, Huhnke RL (2014) Synthesis and evaluation of biochar-derived catalysts for removal of toluene (model tar) from biomass-generated producer gas. Renew Energy 66:346–353. https://doi.org/10.1016/j.renene.2013.12.017

Chaggera HK, Jonesa JM, Pourkashaniana M, Williamsa A, Owenb A, Fynes G (1999) Emission of volatile organic compounds from coal combustion. Fuel 78(13):1527–1538. https://doi.org/10.1016/S0016-2361(99)00050-2

Dai Z, Yu X, Huang C, Li M, Su J, Guo Y, Xu H, Ke Q (2016) Nanocrystalline MnO_2 on an activated carbon fiber for catalytic formaldehyde removal. RSC Adv 6(99):97022–97029. https://doi.org/10.1039/c6ra15463h

Daniel Antonio Aguilera AP, Molina R, Moreno S (2011) Cu–Mn and Co–Mn catalysts synthesized from hydrotalcites and their use in the oxidation of VOCs. Appl Catal B Environ 104(1-2):144–150. https://doi.org/10.1016/j.apcatb.2011.02.019

Delimaris D, Ioannides T (2008) VOC oxidation over MnO_x–CeO_2 catalysts prepared by a combustion method. Appl Catal B Environ 84(1-2):303–312. https://doi.org/10.1016/j.apcatb.2008.04.006

Erik Pitoniak, Chang-Yu Wu, Danielle Londeree DM, Jean-Claude Bonzongo, Kevin Powers, Sigmun W (2003) Nanostructured silica-gel doped with TiO_2 for mercury vapor control J Nanoparticle Res 5:281–292

Evan J. Granite, Henry W. Pennline, Hargis AR (2000) Novel sorbents for mercury removal from flue gas industrial & engineering chemistry research 39:1020–1029

Fei Z, Liu H, Dai Y, Ji W, Chen X, Tang J, Cui M, Qiao X (2014) Efficient catalytic oxidation of HCl to recycle Cl_2 over the CuO–CeO_2 composite oxide supported on Y type zeolite. Chem Eng J 257:273–280. https://doi.org/10.1016/j.cej.2014.07.033

Feng Qu JW, Ningru Xu, Chang Liu, Shuyuan Li, Ning Wang, Wei Qi, Haifeng Li, Chunbao Li, Zhenying Geng YL (2013) WNT3A modulates chondrogenesis via canonical and non-canonical Wnt pathways in MSCs Front Biosci-Landmrk 18:493–503

Fernandez-Martinez PL-M G, Muniategui-Lorenzo S, Prada-Rodr!quez D, Fernandez-Fernandez E (2001) Distribution of volatile organic compounds during the combustion process in coal-fired power stations. Atmos Environ 35:5823–5831

Granite EJ, Pennline HW (2002) Photochemical Removal of Mercury from Flue Gas Industrial & Engineering Chemistry Research 41:5470–5476

Granite Evan J, Henry W. Pennline, Connie Senior, editors and co-authors (2014), Mercury Control for Coal-Derived Gas Streams,Wiley-VCH

Guo J-X, Y-F Q, Shu S, Wang X-J, Yin H-Q, Chu Y-H (2015) Effects of preparation conditions on Mn-based activated carbon catalysts for desulfurization. New J Chem 39(8):5997–6015. https://doi.org/10.1039/c5nj00873e

He C, Shen B, Chen J, Cai J (2014) Adsorption and oxidation of elemental mercury over Ce-MnOx/Ti-PILCs. Environ Sci Technol 48(14):7891–7898. https://doi.org/10.1021/es5007719

He C, Shen B, Li F (2016) Effects of flue gas components on removal of elemental mercury over Ce-MnOx/Ti-PILCs. J Hazard Mater 304:10–17. https://doi.org/10.1016/j.jhazmat.2015.10.044

Hongbo F, Wang X, Wu H, Yin Y, Chen aJ (2007) Heterogeneous uptake and oxidation of so_2 on iron oxides. J Phys Chem 111:6077–6085

Huang H, Hu P, Huang H, Chen J, Ye X, Leung DYC (2014) Highly dispersed and active supported Pt nanoparticles for gaseous formaldehyde oxidation: influence of particle size. Chem Eng J 252:320–326. https://doi.org/10.1016/j.cej.2014.04.108

Ivanov EA, Popova GY, Chesalov YA, Andrushkevich TV (2009) In situ FTIR study of the kinetics of formic acid decomposition on V–Ti oxide catalyst under stationary and non-stationary conditions. Determination of kinetic constants. J Mol Catal A Chem 312(1-2):92–96. https://doi.org/10.1016/j.molcata.2009.07.022

Jin R, Liu Y, Wu Z, Wang H, Gu T (2010) Low-temperature selective catalytic reduction of NO with NH_3 over Mn-Ce oxides supported on TiO_2 and Al_2O_3: a comparative study. Chemosphere 78(9):1160–1166. https://doi.org/10.1016/j.chemosphere.2009.11.049

Konsolakis M, Carabineiro SA, Tavares PB, Figueiredo JL (2013) Redox properties and VOC oxidation activity of Cu catalysts supported on $Ce_{1-x}Sm_x$Odelta mixed oxides. J Hazard Mater 261:512–521. https://doi.org/10.1016/j.jhazmat.2013.08.016

Kwon DW, Seo PW, Kim GJ, Hong SC (2015) Characteristics of the HCHO oxidation reaction over Pt/TiO_2 catalysts at room temperature: the effect of relative humidity on catalytic activity. Appl Catal B Environ 163:436–443. https://doi.org/10.1016/j.apcatb.2014.08.024

Lahousse C, AB, Grange P, Delmon B, Papaefthimiou P, Ioannides T, Verykios X (1998) Evaluation of γ-MnO_2 as a VOC removal catalyst: comparison with a noble metal catalyst. J Catal 178(1):214–225. https://doi.org/10.1006/jcat.1998.2148

Lee H, Park Rs, Lee HW, Hong Y, Lee Y, Park SH, Jung SC, Yoo KS, Jeon JK, Park YK (2016) Adsorptive removal of atmospheric pollutants over Pyropia tenera chars. Carbon Lett 19:79–88. https://doi.org/10.5714/cl.2016.19.079

Li H, Li Y, Wu C-Y, Zhang J (2011a) Oxidation and capture of elemental mercury over SiO_2–TiO_2–V_2O_5 catalysts in simulated low-rank coal combustion flue gas. Chem Eng J 169(1-3):186–193. https://doi.org/10.1016/j.cej.2011.03.003

Li T-Y, Chiang S-J, Liaw B-J, Chen Y-Z (2011b) Catalytic oxidation of benzene over CuO/$Ce_{1-x}Mn_xO_2$ catalysts. Appl Catal B Environ 103(1-2):143–148. https://doi.org/10.1016/j.apcatb.2011.01.020

Li H, Wu S, Wu CY, Wang J, Li L, Shih K (2015) SCR atmosphere induced reduction of oxidized mercury over CuO-CeO_2/TiO_2 catalyst. Environ Sci Technol 49(12):7373–7379. https://doi.org/10.1021/acs.est.5b01104

Liu F, He H, Ding Y, Zhang C (2009) Effect of manganese substitution on the structure and activity of iron titanate catalyst for the selective catalytic reduction of NO with NH_3. Appl Catal B Environ 93(1-2):194–204. https://doi.org/10.1016/j.apcatb.2009.09.029

Liu M, Zhang W, Wang X, Chen L, Wang H, Luo Y, Zhang H, Shen H, Tong Y, Ou L, Xie H, Ye X, Deng C (2016) Mercury release to aquatic environments from anthropogenic sources in China from 2001 to 2012. Environ Sci Technol 50(15):8169–8177. https://doi.org/10.1021/acs.est.6b01386

Ma C, Wang D, Xue W, Dou B, Wang H, Hao Z (2011) Investigation of formaldehyde oxidation over Co_3O_4-CeO_2 and Au/Co_3O_4-CeO_2 catalysts at room temperature: effective removal and determination of reaction mechanism. Environ Sci Technol 45(8):3628–3634. https://doi.org/10.1021/es104146v

Morales M, Barbero B, Cadus L (2006) Total oxidation of ethanol and propane over Mn-Cu mixed oxide catalysts. Appl Catal B Environ 67(3-4):229–236. https://doi.org/10.1016/j.apcatb.2006.05.006

O'Shea VAP, Álvarez-Galván MC, Fierro JLG, Arias PL (2005) Influence of feed composition on the activity of Mn and PdMn/Al_2O_3 catalysts for combustion of formaldehyde/methanol. Appl Catal B Environ 57(3):191–199. https://doi.org/10.1016/j.apcatb.2004.11.001

Peng P-Y, Jin I, Yang TCK, Huang C-M (2014) Facile preparation of hierarchical CuO–CeO_2/Ni metal foam composite for preferential oxidation of CO in hydrogen-rich gas. Chem Eng J 251:228–235. https://doi.org/10.1016/j.cej.2014.04.077

Presto AAG, E.J (2007) Impact of sulfur oxides on mercury capture by activated carbon. Environ Sci Technol 41:6579–6584

Presto AAG, E. J., Karash, A. (2007) Further Investigation of the Impact of Sulfur Oxides on Mercury Capture by Activated Carbon Industrial & Engineering Chemistry Research 46:8273–8276

Qu Y-F, Guo J-X, Chu Y-H, Sun M-C, Yin H-Q (2013) The influence of Mn species on the SO_2 removal of Mn-based activated carbon catalysts. Appl Surf Sci 282:425–431. https://doi.org/10.1016/j.apsusc.2013.05.146

Saha A, Abram DN, Kuhl KP, Paradis J, Crawford JL, Sasmaz E, Chang R, Jaramillo TF, Wilcox J (2013) An X-ray photoelectron spectroscopy study of surface changes on brominated and sulfur-treated activated carbon sorbents during mercury capture: performance of pellet versus fiber sorbents. Environ Sci Technol 47(23):13695–13701. https://doi.org/10.1021/es403280z

Sheng J, Li C, Zhao L, Du X, Gao L, Zeng G (2017) Efficient removal of HCHO from simulated coal combustion flue gas using CuO-CeO_2 supported on cylindrical activated coke. Fuel 197:397–406. https://doi.org/10.1016/j.fuel.2017.02.056

Shiau CY, Ma MW, Chuang CS (2006) CO oxidation over CeO_2-promoted Cu/γ-Al_2O_3 catalyst: effect of preparation method. Appl Catal A Gen 301(1):89–95. https://doi.org/10.1016/j.apcata.2005.11.018

Tang W, Wu X, Li S, Shan X, Liu G, Chen Y (2015) Co-nanocasting synthesis of mesoporous Cu–Mn composite oxides and their promoted catalytic activities for gaseous benzene removal. Appl Catal B Environ 162:110–121. https://doi.org/10.1016/j.apcatb.2014.06.030

Tang S, Yuan D, Zhang Q, Liu Y, Zhang Q, Liu Z, Huang H (2016) Fe-Mn bi-metallic oxides loaded on granular activated carbon to enhance dye removal by catalytic ozonation. Environ Sci Pollut Res Int 23(18):18800–18808. https://doi.org/10.1007/s11356-016-7030-5

Trépanier M, Tavasoli A, Dalai AK, Abatzoglou N (2009) Co, Ru and K loadings effects on the activity and selectivity of carbon nanotubes supported cobalt catalyst in Fischer–Tropsch synthesis. Appl Catal A Gen 353(2):193–202. https://doi.org/10.1016/j.apcata.2008.10.061

Karen J. Uffalussy(2015), Novel capture technologies: non-carbon sorbents and photochemical oxidations, Wiley-VCH, Chapter 21, p. 339–356

Wang Z, Bai Z, Yu H, Zhang J, Zhu T (2004) Regulatory standards related to building energy conservation and indoor-air-quality during rapid urbanization in China. Energy and Buildings 36(12):1299–1308. https://doi.org/10.1016/j.enbuild.2003.09.013

Wang Y, Ge C, Zhan L, Li C, Qiao W, Ling L (2012) MnO_x–CeO_2/activated carbon honeycomb catalyst for selective catalytic reduction of NO with NH3at low temperatures. Ind Eng Chem Res 51(36):11667–11673. https://doi.org/10.1021/ie300555f

Wang XQ, Wang P, Ning P, Ma YX, Wang F, Guo XL, Lan Y (2015) Adsorption of gaseous elemental mercury with activated carbon impregnated with ferric chloride. RSC Adv 5(32):24899–24907. https://doi.org/10.1039/c5ra01011j

Wang Y, Li C, Zhao L, Xie Y, Zhang X, Zeng G, Wu H, Zhang J (2016) Study on the removal of elemental mercury from simulated flue gas by Fe_2O_3-CeO_2/AC at low temperature. Environ Sci Pollut Res Int 23(6):5099–5110. https://doi.org/10.1007/s11356-015-5717-7

Wu H, Li C, Zhao L, Zhang J, Zeng G, Xie Y, Zhang X, Wang Y (2015) Removal of gaseous elemental mercury by cylindrical activated coke loaded with CoO_x-CeO_2 from simulated coal combustion flue gas. Energy Fuel 29(10):6747–6757. https://doi.org/10.1021/acs.energyfuels.5b00871

Wu J, Zhao Z, Huang T, Sheng P, Zhang J, Tian H, Zhao X, Zhao L, He P, Ren J, Gao K (2017) Removal of elemental mercury by Ce-Mn co-modified activated carbon catalyst. Catal Commun 93:62–66. https://doi.org/10.1016/j.catcom.2017.01.016

Xiaolan Tang BZ, Li Y, Xu Y, Xin Q, Shen W (2004) Structural features and catalytic properties of Pt/CeO_2 catalysts prepared by modified reduction-deposition techniques. Catalysis Letters 97:163–169

Xingfu T, Yide X, Shen W (2008) Promoting effect of copper on the catalytic activity of MnO_x–CeO_2 mixed oxide for complete oxidation of benzene. Chem Eng J 144(2):175–180. https://doi.org/10.1016/j.cej.2008.01.016

Xingyi W, Qian K, Dao L (2009) Catalytic combustion of chlorobenzene over MnO_x–CeO_2 mixed oxide catalysts. Appl Catal B Environ 86(3-4):166–175. https://doi.org/10.1016/j.apcatb.2008.08.009

Xu H, Qu Z, Zong C, Huang W, Quan F, Yan N (2015) MnO_x/graphene for the catalytic oxidation and adsorption of elemental mercury. Environ Sci Technol 49(11):6823–6830. https://doi.org/10.1021/es505978n

Yang J, Zhao Y, Ma S, Zhu B, Zhang J, Zheng C (2016) Mercury removal by magnetic biochar derived from simultaneous activation and magnetization of sawdust. Environ Sci Technol 50(21):12040–12047. https://doi.org/10.1021/acs.est.6b03743

Ye Q, Zhao J, Huo F, Wang D, Cheng S, Kang T, Dai H (2013) Nanosized Au supported on three-dimensionally ordered mesoporous β-MnO_2: highly active catalysts for the low-temperature oxidation of carbon monoxide, benzene, and toluene. Microporous Mesoporous Mater 172:20–29. https://doi.org/10.1016/j.micromeso.2013.01.007

You F-T, Yu G-W, Wang Y, Xing Z-J, Liu X-J, Li J (2017) Study of nitric oxide catalytic oxidation on manganese oxides-loaded activated carbon at low temperature. Appl Surf Sci 413:387–397. https://doi.org/10.1016/j.apsusc.2017.04.044

Zhang J, Jin Y, Li C, Shen Y, Han L, Hu Z, di X, Liu Z (2009) Creation of three-dimensionally ordered macroporous Au/CeO_2 catalysts with controlled pore sizes and their enhanced catalytic performance for formaldehyde oxidation. Appl Catal B Environ 91(1-2):11–20. https://doi.org/10.1016/j.apcatb.2009.05.001

Zhang G, Li Z, Zheng H, Fu T, Ju Y, Wang Y (2015) Influence of the surface oxygenated groups of activated carbon on preparation of a nano Cu/AC catalyst and heterogeneous catalysis in the oxidative carbonylation of methanol. Appl Catal B Environ 179:95–105. https://doi.org/10.1016/j.apcatb.2015.05.001

Zhang J, Li C, Zhao L, Wang T, Li S, Zeng G (2017) A sol-gel Ti-Al-Ce-nanoparticle catalyst for simultaneous removal of NO and Hg0 from simulated flue gas. Chem Eng J 313:1535–1547. https://doi.org/10.1016/j.cej.2016.11.039

Zhao L, Li C, Zhang J, Zhang X, Zhan F, Ma J, Xie Y, Zeng G (2015) Promotional effect of CeO_2 modified support on V_2O_5–WO_3/TiO_2 catalyst for elemental mercury oxidation in simulated coal-fired flue gas. Fuel 153:361–369. https://doi.org/10.1016/j.fuel.2015.03.001

Zhao L, Li C, Li S, Wang Y, Zhang J, Wang T, Zeng G (2016a) Simultaneous removal of elemental mercury and NO in simulated flue gas over V_2O_5/ZrO_2-CeO_2 catalyst. Appl Catal B Environ 198: 420–430. https://doi.org/10.1016/j.apcatb.2016.05.079

Zhao L, Li C, Zhang X, Zeng G, Zhang J, Xie Y (2016b) Oxidation of elemental mercury by modified spent TiO_2-based SCR-$DeNO_x$ catalysts in simulated coal-fired flue gas. Environ Sci Pollut Res Int 23(2):1471–1481. https://doi.org/10.1007/s11356-015-5143-x

Zheng-Hong Huang FK, Zheng Y-P, Yang J-B, Liang K-M (2002) Adsorption of trace polar methy-ethyl-ketone and non-polar benzene vapors on viscose rayon-based activated carbon fibers Carbon 40:1363–1367